



HAL
open science

Microstructure Evolution and Mechanical Properties of AISI 430 Ferritic Stainless Steel Strengthened Through Laser Carburization

Zhige Wang, Justin Dirrenberger, Pierre Lapouge, Sébastien Dubent, Hamza
Jabir, Vincent Michel

► **To cite this version:**

Zhige Wang, Justin Dirrenberger, Pierre Lapouge, Sébastien Dubent, Hamza Jabir, et al.. Microstructure Evolution and Mechanical Properties of AISI 430 Ferritic Stainless Steel Strengthened Through Laser Carburization. *Journal of Engineering Materials and Technology*, 2022, 144 (4), pp.041005. 10.1115/1.4055025 . hal-03753543

HAL Id: hal-03753543

<https://hal.science/hal-03753543v1>

Submitted on 18 Aug 2022

HAL is a multi-disciplinary open access archive for the deposit and dissemination of scientific research documents, whether they are published or not. The documents may come from teaching and research institutions in France or abroad, or from public or private research centers.

L'archive ouverte pluridisciplinaire **HAL**, est destinée au dépôt et à la diffusion de documents scientifiques de niveau recherche, publiés ou non, émanant des établissements d'enseignement et de recherche français ou étrangers, des laboratoires publics ou privés.

Zhige Wang

PIMM, Arts et Metiers Institute of Technology,
CNRS, Cnam, HESAM Universite,
151 Boulevard de l'Hopital,
Paris 75013, France
e-mail: zhige.wang@ensam.eu

Justin Dirrenberger¹

PIMM, Arts et Metiers Institute of Technology,
CNRS, Cnam, HESAM Universite,
151 Boulevard de l'Hopital,
Paris 75013, France
e-mail: justin.dirrenberger@ensam.eu

Pierre Lapouge

PIMM, Arts et Metiers Institute of Technology,
CNRS, Cnam, HESAM Universite,
151 Boulevard de l'Hopital,
Paris 75013, France
e-mail: pierre.lapouge@ensam.eu

Sébastien Dubent

PIMM, Arts et Metiers Institute of Technology,
CNRS, Cnam, HESAM Universite,
151 Boulevard de l'Hopital,
Paris 75013, France
e-mail: sebastien.dubent@lecnam.net

Hamza Jabir

PIMM, Arts et Metiers Institute of Technology,
CNRS, Cnam, HESAM Universite,
151 Boulevard de l'Hopital,
Paris 75013, France
e-mail: hamza.jabir@ensam.eu

Vincent Michel

PIMM, Arts et Metiers Institute of Technology,
CNRS, Cnam, HESAM Universite,
151 Boulevard de l'Hopital,
Paris 75013, France
e-mail: vincent.michel@ensam.eu

Microstructure Evolution and Mechanical Properties of AISI 430 Ferritic Stainless Steel Strengthened Through Laser Carburization

Carburization assisted by laser processing is a promising method to strengthen metallic materials. Direct laser beam carburization is implemented for the first time on thin AISI 430 ferritic stainless steel (FSS) sheets with graphite coating under different conditions. Microstructural morphology, phase constitution, carbon content, microhardness, and tensile behavior are investigated to evaluate the laser carburization effect. The carburized zone presents different morphologies according to the linear energy density of the laser beam. The least carbon content is around 0.4 wt% in the carburized zone where austenite becomes the leading phase. Delta ferrite is found in a cellular carburized area, which resembles a duplex microstructure. The hardness of carburized zone has been at least increased by 130%, the yield strength and ultimate tensile strength of a fully carburized sample can be increased by respectively 90% and 85%. This hardening effect is driven by the precipitation of carbides formed during solidification offering pinning points for dislocations and grain boundaries. These improvements could be useful to modify locally ferritic stainless steel to meet industrial needs such as wear-resistant surfaces.
[DOI: 10.1115/1.4055025]

Keywords: carburization, laser processing, ferritic stainless steel, hardening, materials processing, mechanical behavior, metals, polymers, ceramics, intermetallics, microstructure property relationships, plastic behavior

1 Introduction

Ferritic stainless steels (FSS) are extensively used in different industries for their appropriate properties, such as high corrosion resistance, thermal conductivity, ductility, and low thermal expansion, and their less expensive price compared to austenitic stainless steels. However, relatively lower fracture strength and work hardening rate restrict the applications of FSS [1]. To counteract these downsides, some authors proposed surface hardening treatments to strengthen the surface layer to adapt to specific needs, e.g., self-quenching (SQ) [2], carburization and nitriding [3]. Traditionally surface carburization and nitriding are obtained by gas treatment in the furnace and plasma technique, which take usually several to hundreds of hours [4]. It enables the introduction of carbon or nitrogen atoms into the metallic matrix to form a solid solution or carbides/nitrides to increase the surface hardness and wear resistance [5].

As an alternative to bulk processing, laser heat treatment of metallic materials has developed steadily in recent years partly

due to its rapid heating and cooling rates. As a matter of fact, by controlling peak temperatures and interaction times, different modifications can be achieved according to industrial needs, such as softening [6,7] or hardening [8]. Laser surface carburization and nitriding is a novel less time-consuming method compared to classical methods [4]. Studies were carried out on laser irradiation on ferrous or other metallic materials in carburizing atmosphere of alkanes or CO₂ [9], which were proven efficient to improve the surface mechanical properties. The high energy intensity in a reactive atmosphere generates a series of intricate transformations which involve different mechanisms such as absorption, diffusion, and convection [5,10].

Another carburization method consists of heating the material surfaces coated by graphite above critical temperatures, or even melting temperature, by laser to diffuse carbon atoms [10]. Saleh et al. [11] implemented a carburization process on Ti-6Al-4V alloy by laser irradiation on graphite coat and found that the use of graphite powder increased the microhardness notably by forming carbide particles and dendrites. A carbonitriding process by Seo et al. [12] was carried out with the same alloy in a nitrogen shielding gas and the result showed that the laser hardening effect was more enhanced by carbon/nitrogen-rich phases. A similar study by Makuch et al. [13] showed that the wear resistance of laser-carburized titanium and its alloys increased significantly.

¹Corresponding author.

Direct laser carburization (LC) has also been studied on different ferrous materials. Carbon coat increases the laser beam absorption, which leads to a more elevated temperature in the irradiated area, thus crystal nucleation and growth are more favored and numerous carbides are formed [14,15]. Due to the abrupt temperature gradient between the molten pool and substrate, various microstructures can be achieved in different zones [16]. Katsamas and Haidemenopoulos [17] reported laser carburization on 15CrNi6 low-alloy steel by both solid-state carbon diffusion and surface remelting which incorporates carbon atoms. According to different process parameters, the carburized layer exhibited a microhardness from 2.5 to 4 times higher compared to the substrate. A carbon nanotube slurry coat was studied by Yao et al. [18] on medium carbon steel and mild steel to be compared with graphite coat during laser carburization. Both coats yielded a carburized hardening layer with comparable peak values, but the carbon nanotube presented a higher dissolution into the substrate.

Most of the existing studies on the carburization of stainless steel are focused on austenitic and martensitic grades in a gaseous or plasma environment at a relatively lower temperature than that of direct laser carburization. According to the initial microstructures, this low temperature surface carburization results in expanded austenite or martensite, which is a solid solution supersaturated in carbon under metastable equilibrium conditions, thus an obvious increase in hardness and wear resistance of the surface [19,20]. Even though certain stainless steel grades present higher kinetics during the treatment, the strengthened layers are often limited in thickness from a few micrometers to tens of micrometers after hours of treatment [21], which is rather inefficient for surface strengthening. Nevertheless, direct laser beam heat treatment allows a deeper and faster penetration due to its high energy density, which leads to a thicker strengthened surface.

Because ferritic grades are not usually considered as heat treatable, studies on the carburization of FSS are very limited. In the present work, direct carburization assisted by a continuous-wave laser is investigated for the first time on FSS coated with graphite spray. AISI 430 is chosen for this study, it is one of the most widely used FSS grades in the industry. Microstructure and mechanical properties are examined on fully treated specimens to evaluate the laser carburization efficiency and the influence of treatment parameters is discussed. Results are compared with the authors' earlier work [22], which unveils the direct hardening effect of laser heat treatment on AISI 430 without graphite coating with the same experimental parameters.

2 Material and Experimental Procedure

AISI 430 sheets of 0.5 mm thickness are adopted for this study. It is to note that this thickness is chosen on purpose to achieve a higher ratio of the carburized zone to the bulk thickness. The initial surface

state is mirror-polished on both sides, but in order to increase the cohesiveness of graphite powder, the sheets are sand-blasted and cleaned with ethanol. A commercial painting graphite powder is sprayed evenly on both surfaces until they are fully covered and then dried in air for 24 h before laser irradiation.

Figure 1(a) shows the laser treatment platform. Two lasers are installed on each side to be used either simultaneously or separately in order to compare the effect of one-side treatment and double-side treatment. The two lasers available for this study are a single-mode 500 W fiber laser from SPI (surface A) at a wavelength of 1080 nm and a multimode 110 W laser diode from DILAS (surface B) at a wavelength of 980 nm. The sheets are fixed in an aluminum alloy frame to avoid thermal deformation during the treatment. The frame is fastened on a robotic arm that can move with a pre-programmed trajectory, illustrated in Fig. 1(b). Argon shielding gas is used to reduce oxide formation on the sheet surfaces at high temperature. The spot size is defocused at 1 mm for surface A and surface B is fixed at the focus distance, where the spot size is 1.2 mm. Even though the theoretic spot size on surface B is larger than surface A, microstructural results from the authors' earlier study [22] show that the treated zone is almost symmetric on two sides. This is due to different intensity profiles for the two lasers.

Laser treatment parameters are shown in Table 1. For a total linear energy density (LED), irradiations from single laser and double laser treatments are compared. The velocity (v) of the robot arm is fixed at 10 mm/s. SQ specimens without graphite coating are treated in the same conditions to compare the LC effect. The temperature evolutions of single laser treatment at 150 W and 200 W are measured for every millisecond with several type K thermocouples welded on the backside surface (surface B). The temperature on the laser side is simulated by the finite element method using the software COMSOL MULTIPHYSICS. Both laser beams are modeled as Gaussian beams.

Microstructural observations are realized on the cross section before and after laser treatment using an optical microscope and scanning electron microscope (SEM) equipped with energy dispersive X-ray spectrometry (EDS) and electron backscatter diffraction (EBSD) detector. Before the observations, the samples are prepared by grinding with silicon carbide abrasive papers with grit sizes of 240, 400, 800, and 1000 followed by cloth polishing using 9, 3, and 1 μm diamond suspension solutions and finished by 0.04 μm colloidal silica suspension (OP-S). The treated samples are etched in diluted aqua regia (15 ml HCl, 5 ml HNO₃, and 100 ml distilled water) for about 20 s to reveal the microstructure. The etching solution outlines the grain boundaries and carbides [23]. Phase identification is carried out using EBSD analysis, three phases: bcc Fe, fcc Fe, and cubic Cr₂₃C₆ are selected for indexing.

To determine the present phases on surface layers of samples after removing the oxidation, X-ray diffraction analysis was conducted on a PANalytical X'Pert diffractometer. A cobalt anode

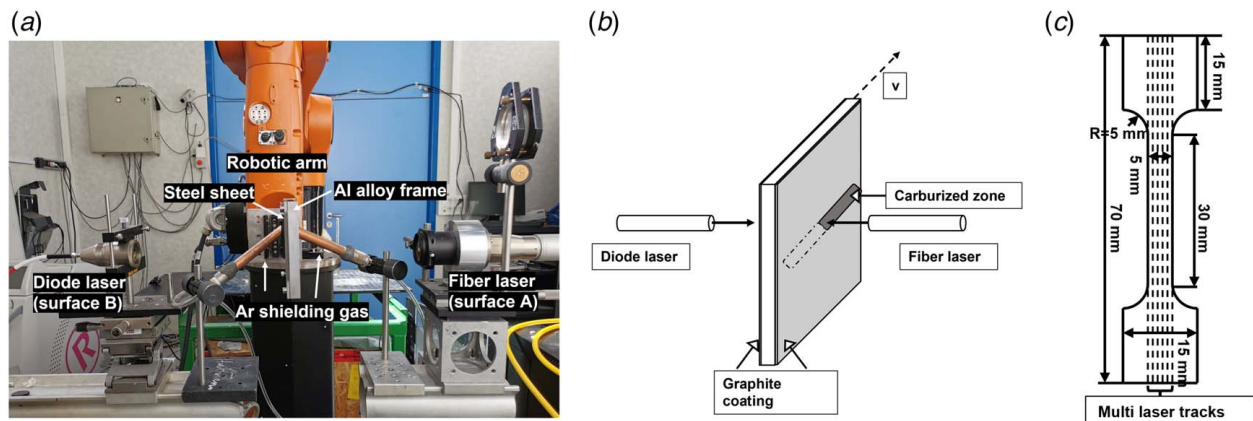


Fig. 1 (a) Laser treatment platform, (b) schematic configuration of laser carburization, and (c) fully treated sample dimension

Table 1 Laser treatment parameters

Type of process on SQ and LC samples	Power (W)	Velocity (mm/s)	Linear energy density P/v (kJ/m)
1—Single laser	150	10	15
2—Double laser	75 + 75	10	15
3—Single laser	200	10	20
4—Double laser	100 + 100	10	20

Table 2 Chemical composition (wt%) of the stainless steel AISI 430 sample

C	Si	Mn	Cr	Ni	P	Fe
0.026	0.30	0.50	18.70	0.14	0.03	Bal.

was used emitting mainly through the $K\alpha$ ray at a wavelength of 0.179 nm. The 2θ diffraction data were collected from 40 deg to 140 deg with a step size of 0.025 deg with an integrated acquisition time of 300 s. All scans were carried out in continuous mode.

To investigate the carburization efficiency, the chemical compositions of both as-received material and fully treated samples through the thickness are measured by glow discharge optical emission spectrometry (GD-OES), using a Horiba JY 10,000 RF spectrometer equipped with a 4 mm diameter anode. The argon pressure and RF power parameters, chosen to obtain a flat crater bottom during the erosion of the treated samples, were 750 Pa and 40 W respectively. Preliminary tests are carried out on both treated and untreated samples for 20 min in order to achieve a deep enough crater to determine the average sputtering rate of the surface, which is 4.3 $\mu\text{m}/\text{min}$. The element composition of as-received material is shown in Table 2. The carbon contents of laser-carburized samples are specifically followed during the analysis.

Vickers microhardness tests are realized along the laser track center on the cross section with a force of 50 gf and a load time of 10 s. Tensile tests are carried out on LC, SQ samples, and as-received samples with dimensions shown in Fig. 1(c). For LC and SQ samples, five laser tracks were applied with an interval of

1 mm, which corresponded to a gage section fully covered in theory. After each track, there is a cooling time of at least 30 s in order to minimize the reheat of adjacent tracks.

3 Results

3.1 Temperature Evolution. Figure 2 depicts the experimental temperature evolution and numerical approach during single laser treatment in the beam center on the back surface for both SQ and LC processes. For the same process, the peak temperature is more elevated with a higher LED. And for a given LED, peak temperatures of the LC process are superior to those of the SQ process as graphite coating has a greater absorptivity and favors the heat transfer between the laser beam and the metallic substrate [12].

For modeling parameters, specific heat capacity c_p and thermal conductivity λ of AISI 430 are calculated using Eqs. (1) and (2), where T is the instant temperature ($^{\circ}\text{C}$). The fusion point is set at 1698 K, and the latent fusion heat is 285 kJ/kg. A heat transfer coefficient of $200 \text{ W} \cdot \text{m}^{-2} \cdot \text{K}^{-1}$ between the irradiated substrate and the environment is included in the consideration of shielding gas flux [24]. The absorption coefficients for SQ and LC samples are trimmed to adjust to the experimental results, taken as 0.41 and 0.52 respectively. Critical temperatures are calculated according to the main alloying elements [25,26], in this study, $Ac1 = 1148 \text{ K}$, $Ac3 = 1355 \text{ K}$, and $Ms = 841 \text{ K}$.

$$c_p = 450 + 0.280 \times T - 2.91 \times 10^{-4} T^2 + 1.34 \times 10^{-7} T^3 \text{ [J} \cdot \text{kg}^{-1} \cdot \text{K}^{-1}] \quad (1)$$

$$\lambda = 14.6 + 1.27 \times 10^{-2} T \text{ [W} \cdot \text{m}^{-1} \cdot \text{K}^{-1}] \quad (2)$$

The same parameters are used to estimate the temperature evolution under all conditions, as shown in Fig. 3. All results present an asymmetric form where the heating rate is higher than the cooling one. The influence of LED and graphite coating is similar to what is shown in Fig. 2. For all direct irradiated side, the peak temperatures exceed $Ac3$, and the melting point is attained except for LC samples at 15 kJ/m. At 20 kJ/m for both cases, the peak temperatures on the direct irradiated sides of LC and SQ process are very close, less than 10 K, because of the latent fusion heat. For double laser treatment in Fig. 3(b), two irradiated sides present

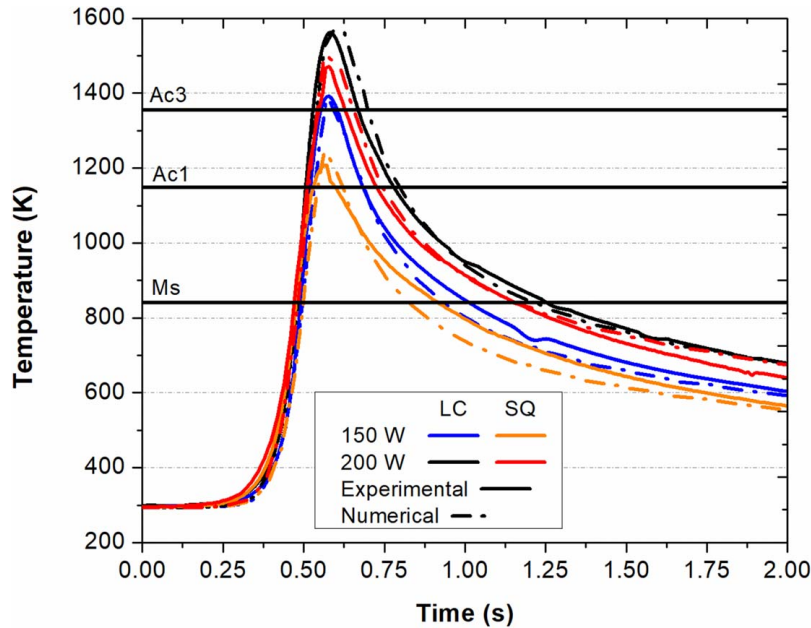


Fig. 2 Comparison between experimental results and numerical simulations of temperature evolutions on the surface B (indirect irradiated side) under different conditions

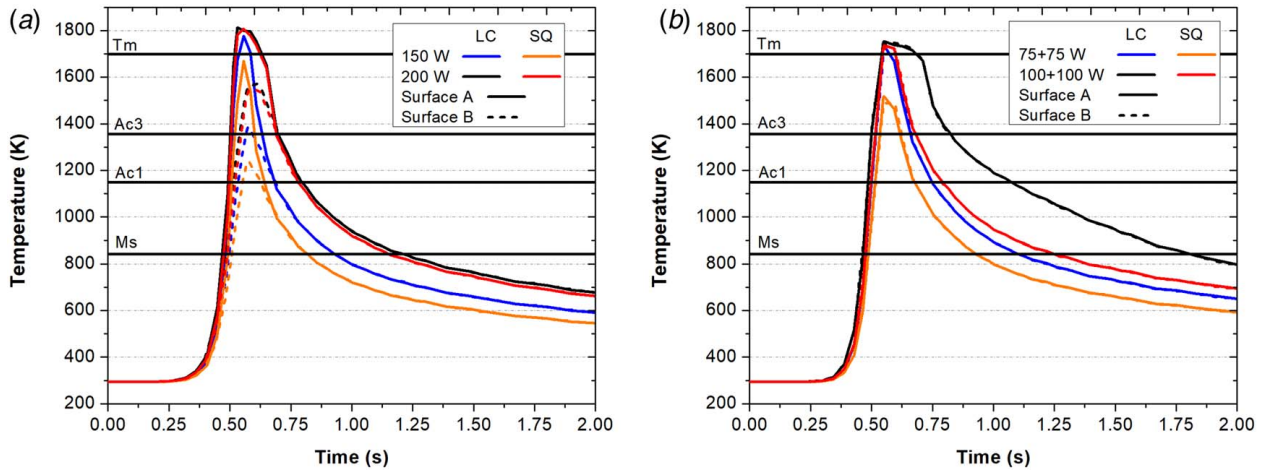


Fig. 3 Numerical simulations of temperature evolution at the beam center of two surfaces for both (a) single and (b) double laser treatments

alike aspects and slower cooling process compared to single laser treatment. The LC sample at 100 W from both sides generates a longer maintain duration above the melting point and the melting pool size is wider than other conditions because of higher LED and absorption rate. Thus, its cooling rate is obviously lower than the others, but still over 800 K/s.

The authors' earlier work [22] has already proven that the double laser treatment yields a more uniform temperature field at the beam center through the thickness with the same LED.

3.2 Microstructure Analysis and Phase Identification.

As-received AISI 430 in Fig. 4(a) presents completely equiaxed ferritic grains with uniformly distributed fine intragranular carbides.

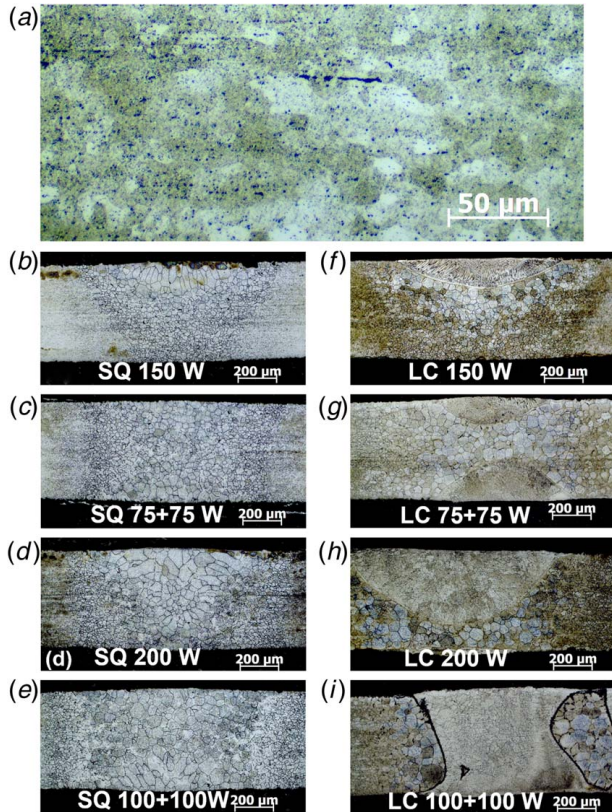


Fig. 4 General section microstructure of (a) as-received material, (b)–(e) SQ samples, and (f)–(i) LC samples

Figures 4(b)–4(e) reveal the section microstructures of SQ samples and LC samples (Figs. 4(f)–4(i)) with different laser parameters. The authors' earlier study [22] shows that SQ samples exhibit dramatic grain coarsening with the increase of LED and martensite formation occurs due to rapid cooling both intergranularly and intragranularly. And compared to single laser treatment, double laser treatment achieves a more uniform microstructure evolution through the thickness due to a smaller temperature gradient because both surfaces are irradiated.

With the same LED, the LC samples exhibit a wider and deeper melting pool because graphite increases the laser absorption rate and thus improves the coupling efficiency between the laser beam and metal substrate [27]. While SQ samples present a consistent microstructure evolution from laser treated zone, in some cases fusion zone (FZ), to heat affected zone (HAZ), LC samples show a clear boundary between carburized zone and HAZ. The average grain sizes of the treated zones are reported in Table 3. The grains of LC samples are finer than SQ samples due to the pinning effect at grain boundaries by carbon atoms. Similar to SQ samples, the grain sizes increase the higher LED and for the same LED, double laser treatment yields a smaller grain size than single one.

In the carburized zone, two typical microstructures are identified as shown in Fig. 5. With a relatively lower LED at 15 kJ/m for both single and double laser treatments, the carburized zone consists of dendrite grains mostly. In Fig. 5(a), equiaxed dendrites are formed near the surface and columnar dendrites are formed in the adjacent layer in FZ. Inside the dendritic grains, alloy elements exist in solid solution. At 20 kJ/m for both single and double laser treatments, the carburized zone is dominated by cellular grains with fine equiaxed grains in the center and columnar grains along the solidification direction of FZ (Figs. 4(h) and 4(i)). Numerous carbides of around 1 μm in diameter are observed inside the grains and at the grain boundaries. But it is to note that the presence of these two kinds of microstructure is not contradictory as they can be found in the same FZ. In Fig. 5(a), even though the microstructure is mostly dendritic, several cellular grains are formed below the columnar dendrites near the interface between FZ and HAZ. Similarly, small quantities of columnar dendrites can be found in the carburized area near the surface when a higher LED is applied.

Scanning electron microscope observation is carried out using both secondary electron signal (SE) and backscattered electron signal (BSE) to investigate dendritic and cellular grains. Figure 6(a) presents short dendritic grains by SE signal, and Fig. 6(b) shows the same area by BSE signal, where the interdendritic regions appear darker than dendrites. This signifies these regions may be richer in C and Cr and poorer in Fe. Zone A is submitted to EDS mapping analysis in Cr, Fe, and C content. Figure 7 confirms

Table 3 Mechanical properties and morphology of as-received material and laser treated samples

	Power (W)	Ys (MPa)	UTS (MPa)	ϵ_u	Grain size (μm)	Morphology
As-received	—	346 ± 12	503 ± 15	$19.39 \pm 0.07\%$	11.2 ± 0.5	Equiaxed grains
	150	458 ± 53	571 ± 49	$14.62 \pm 0.09\%$	32.8 ± 6.7	
SQ sample	75 + 75	488 ± 24	623 ± 20	$15.54 \pm 0.17\%$	22.3 ± 2.8	Coarsening grains
	200	497 ± 10	650 ± 16	$13.85 \pm 1.82\%$	33.9 ± 5.3	
	100 + 100	540 ± 18	702 ± 18	$13.67 \pm 1.42\%$	32.2 ± 1.9	
LC sample	150	565 ± 19	711 ± 19	$4.86 \pm 0.54\%$	4.7 ± 0.5	Dendrite-dominated
	75 + 75	659 ± 26	773 ± 11	$2.57 \pm 0.35\%$	3.9 ± 0.6	
	200	638 ± 20	827 ± 21	$5.63 \pm 0.72\%$	17.6 ± 1.5	Cellular-dominated
	100 + 100	667 ± 22	923 ± 39	$3.47 \pm 0.53\%$	13.5 ± 1.9	

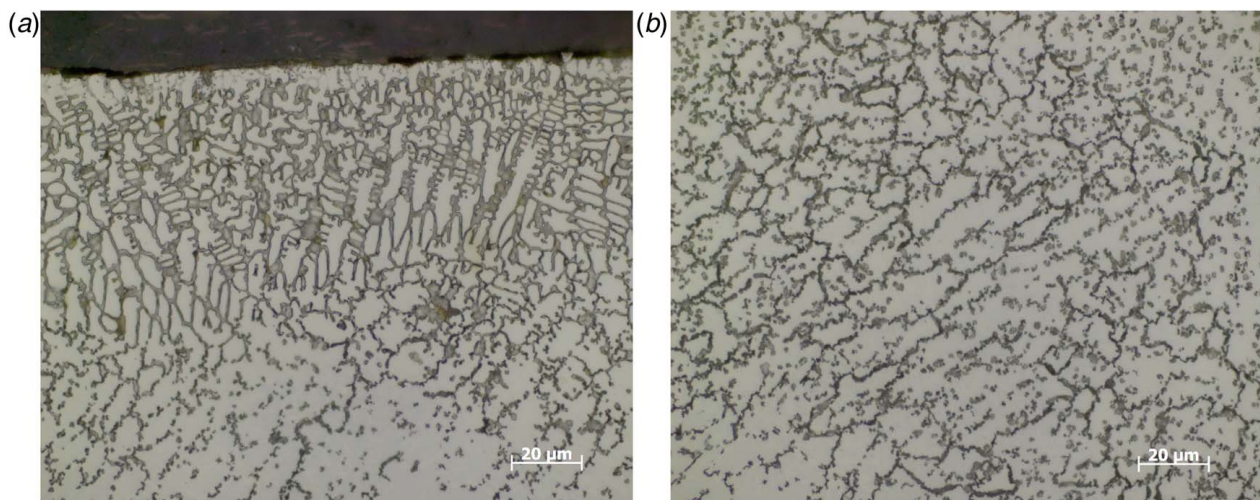
qualitatively that interdendritic regions contain more Cr and C than dendritic regions, but less Fe, which implies element segregation upon solidification. Figure 6(c) shows cellular grains in high magnification, where the bright lines are grain boundaries, and Fig. 6(d) is this region by BSE signal. The darker grain boundaries and small discontinuous precipitations inside grains suggest that the C and Cr content in these parts are more elevated than the matrix.

The microstructure of the interdendritic region in Fig. 6(a) is zoomed in Fig. 8. The interior presents a eutectic morphology, whose average lamellar spacing is less than 100 nm. Solidification begins by forming dendritic austenitic grains, excess carbon atoms are separated out to the left liquid phase and concentrate between dendrites. As Cr has a higher solubility in the liquid γ phase than in solid [28], Cr atoms are also segregated to the liquid phase and accumulate in interdendritic regions with C atoms. The interdendritic region seems to solidify at the latest to be a eutectic structure containing carbides and γ/α phases, which resembles the results of the study in Ref. [27] of laser-carburized austenitic stainless steel.

Figure 9 reveals an EBSD examination of the microstructures introduced in Fig. 5, generated with double lasers at different LEDs. Figures 9(a) and 9(c) show the inverse pole figure (IPF) of the global microstructure at 15 kJ/m and 20 kJ/m, Figs. 9(b) and 9(d) are the magnified carburized zone respectively. Figures 9(e)–9(h) are corresponding phase distribution map. In both two cases, the HAZ presents similar coarsened ferritic grains with a small amount of retained austenite at grain boundaries. Excess carbon atoms accumulate at the interface between carburized zone and HAZ, and therefore form a complex band which is difficult to identify. But due to different cooling rates and carbon concentrations, the carburized zone at different LEDs manifests dissimilar morphology.

In the carburized zone at 15 kJ/m, the dendritic region is an austenitic solid solution and the interdendritic region is rather complicated to detect because of the extra fine lamellar structure and limited resolution of EBSD step size. A tiny amount of ferrite is identified in the interdendritic area, so the eutectic lamellar structure is likely to contain chromium carbides and α -Fe. Dendrites within the same prior austenite grain solidify in the same preferred orientation. At 20 kJ/m, the carburized zone consists mostly of cellular austenitic matrix with intergranular and intragranular island-like mixture of carbides and α -Fe. Similarly, the nature of chromium carbides in this mixture is also hard to index as for the former interdendritic region. It is worth noting that vermicular ferritic grains are found to be surrounded by austenite near the interface between FZ and HAZ. It concerns δ -ferrite issued from the liquid phase directly, which remains stable in a large temperature range within high-alloy stainless steel welds [29]. The crystallographic orientation of cellular grains is more randomly distributed compared to dendritic grains.

Figure 10 compares the XRD spectra of the surface layer on the as-received material and samples treated under different conditions and their phase composition. The diffraction peaks of the as-received material correspond to a single α -ferrite phase. After laser treatment without graphite, similar peaks are detected on the SQ sample and also a small amount of retained austenite (2.2%) appears, which is formed between coarsening ferritic grains upon rapid cooling. However, α' martensite and α -ferrite peaks cannot be distinguished. The patterns of LC samples contain strong peaks of γ austenite, and the ferrite peaks are much weaker, which indicates that austenite becomes the leading phase after carburization. The relative difference in austenitic peak intensities between LC samples with different LEDs may have resulted from preferred orientation under different cooling rates. Carbides

**Fig. 5 Optical micrographs of the sample treated at: (a) 75 W on both sides and (b) 100 W on both sides**

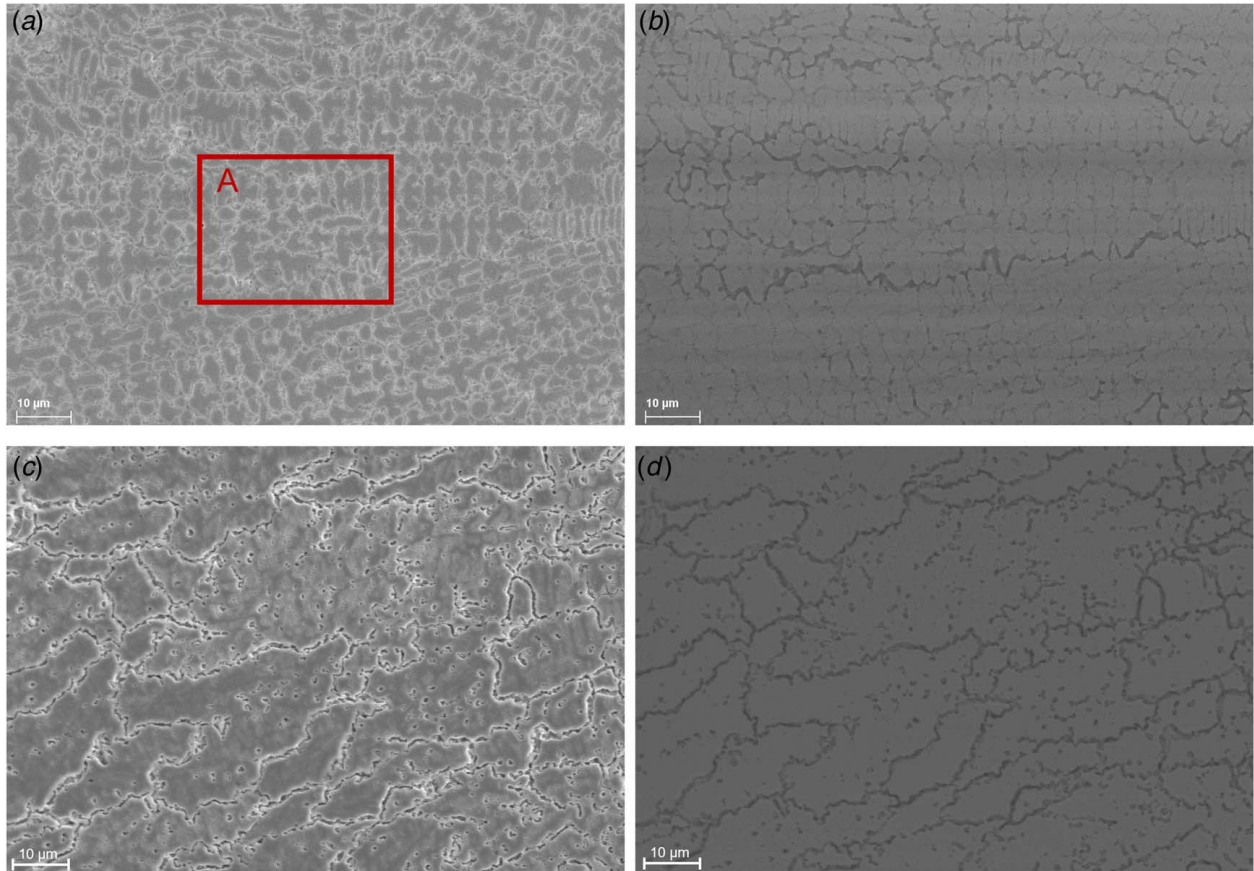


Fig. 6 SEM images of LC samples at (a) and (b) 75 W on both sides, (c) and (d) 100 W on both sides, (a) and (c) SE signal, (b) and (d) BSE signal

cannot be detected in none of the samples owing to the low percentage and weak intensities.

3.3 Carbon Content. The carbon mass content is difficult to be determined through the EDS analysis because the carbon peak has low energy, it is measured by GD-OES through the whole thickness to evaluate the carburizing efficiency. The as-received material contains about 0.026 wt% of carbon and the SQ samples show no evident changes in carbon content after laser treatment. The evolution in C wt% in LC samples is described in Fig. 11. It is noteworthy that since the measurements are taken on a 4 mm diameter surface of fully treated samples containing multi-laser tracks, Fig. 11 does not represent the exact mass fraction of carbon in the carburized region but a lower one because of the uncovering regions between tracks whose carbon content equals to that of as-received material. The results near the irradiated surface are closer to the real mass fractions of C as the uncovering regions are thinner.

With all chosen parameters, laser treatment is efficient to introduce carbon into the low carbon matrix with different depths from the irradiated surface. In the HAZ where grain coarsening and martensite formation happen, C wt% remains the same with the base material. The C wt% at the surface A: 75 W + 75 W > 150 W > 200 W > 100 W + 100 W, from the section microstructures in Fig. 4, a smaller depth of carburized region leads to a more important carbon mass fraction. A complete FZ through the whole thickness by 100 W from both surfaces yields an almost stable C wt% in the bulk, around 0.4%. The asymmetry aspect of C wt% of two irradiated surfaces may be due to the different intensity distributions of laser beams. The higher C wt% (>0.8%) within lower LED 15 kJ/m treated samples confirms the large quantity of interdendritic eutectic microstructures in Fig. 5(a), and the relatively lower one (<0.8%) by 20 kJ/m results in a cellular-dominated microstructure in Fig. 5(b).

3.4 Microhardness. Vickers microhardness tests are taken along the laser track center through the thickness of the sample under different conditions, the results are shown in Fig. 12(a) (single laser treatment) and Fig. 12(b) (double laser treatment). All treatments led to a more important hardness compared to that of as-received material, which is around 160 Hv. For both single and double laser treatments, with the same LED, LC samples exhibit a much more elevated hardness than SQ samples in the fusion zone. Higher LED increases the peak hardness of the fusion zone for SQ samples because more martensite and carbides are formed. But for LC samples, a relatively lower LED yields a shallower but much more hardened carburized region.

For single laser treatment in Fig. 12(a), the hardness decreased from the irradiated side for both SQ and LC samples, but the reduction for LC samples is more dramatic. The highest value is found in the fusion zone at 150 W, 469 Hv. At 200 W, a deeper zone is carburized but it exhibits a lower peak value (380 Hv). Hardness values in the HAZ under the same LED are close in this case because the peak temperatures in HAZ do not differ much from each other. For double laser treated samples in Fig. 12(b), an FZ through the whole thickness is achieved by 100 W from both sides, so the hardness does not evolve much, around 380 Hv and 300 Hv for LC and SQ samples respectively. On the contrary, 75 W from both sides creates a much harder surface (450 Hv), and the values in the adjacent HAZ area are close to SQ samples. Comparing dendritic and cellular grains formed at different LEDs, it can be concluded that the former processes a much more important microhardness than the latter.

3.5 Tensile Test. Figure 13 depicts the uniaxial stress-strain behavior of SQ and LC samples in different conditions, and the mechanical properties are summarized in Table 3. The authors' earlier work [22] reveals that for SQ samples, the increase in

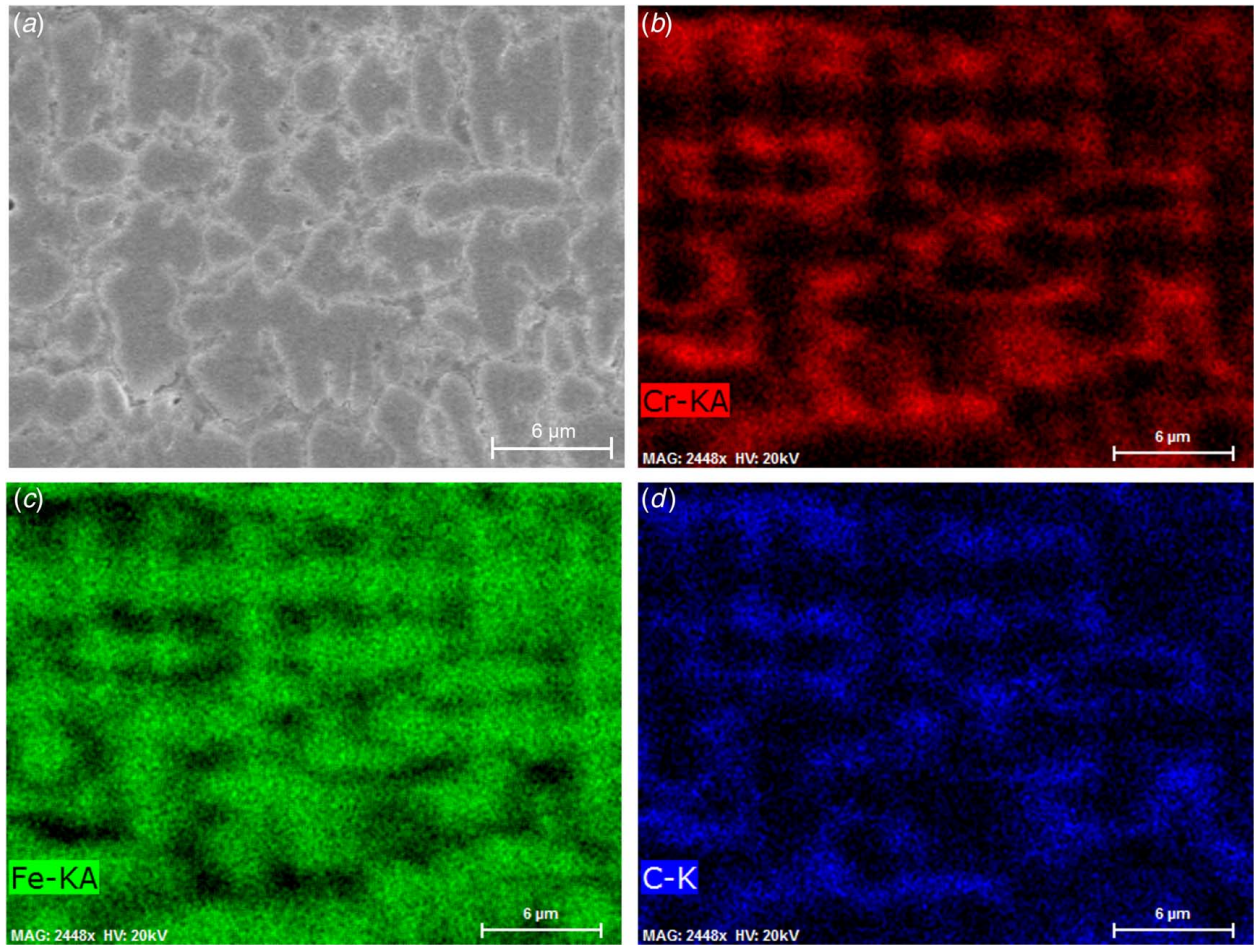


Fig. 7 EDS mapping of the dendritic microstructure of samples treated at 75 W on both sides: (a) SEM image by SE signal, (b) Cr, (c) Fe, and (d) C

LED results in higher yield stress ($\sigma_{0.2\%}$) and ultimate tensile strength (UTS) because more carbides and martensite are formed. And for the same LED, double laser treatment yields a higher $\sigma_{0.2\%}$ and UTS because of more uniform temperature field through the sample thickness. The highest value for $\sigma_{0.2\%}$ and UTS is 579 and 702 MPa at 100 W from both sides compared to 350 MPa and 500 MPa for the as-received material. The uniform plastic deformation (ϵ_u) is reduced from 19.5% to around 14% for the SQ samples.

The LC samples present quite different characteristics. Similar to SQ samples, both increases in LED and double laser treatment lead to higher $\sigma_{0.2\%}$ and UTS due to the expansion of carburized zone.

Compared to SQ samples under the same condition, LC samples have a more elevated $\sigma_{0.2\%}$ and UTS due to the large quantity of austenite and carbides formed in the carburized zone, at most 667 MPa and 923 MPa for 100 W from both sides because a fully carburized region is formed through the whole thickness, which is 90% and 85% more than the as-received material. But the carburization deteriorates severely the ductility, ϵ_u is less than 6% with all chosen parameters. It is worth noticing that higher LED presents a slightly better ϵ_u , which can be explained by the cellular-microstructure, which is less fragile than the dendritic microstructure.

4 Discussion

With chosen parameters, both SQ and LC processes change visibly the microstructure in FZ and HAZ compared with the as-received material. SQ process yields a continuous FZ and HAZ with ferritic grain coarsening and a small amount of martensite formation by rapid heating and cooling, which is discussed thoroughly in the authors' earlier work [22]. During LC process, graphite on the surface is introduced into the molten pool and mixed by Marangoni flow [30], and during the cooling cycle, the molten pool forms a carburized area whose morphology depends strongly on the LED. LC process generates a clear interface between FZ and HAZ by a planar solidification band at the edge of carburized FZ, where the excess carbon atoms cannot further dissolve into HAZ and accumulate. The HAZ presents similar aspects to the SQ samples, a dramatic grain coarsening and a small amount of martensite formation, which is more severe with the increase of LED.

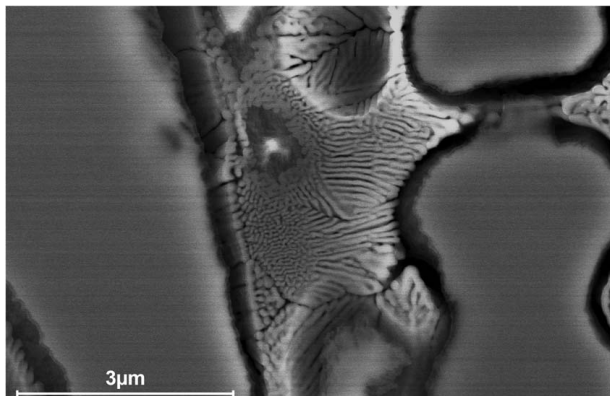


Fig. 8 SEM image of an interdendritic region

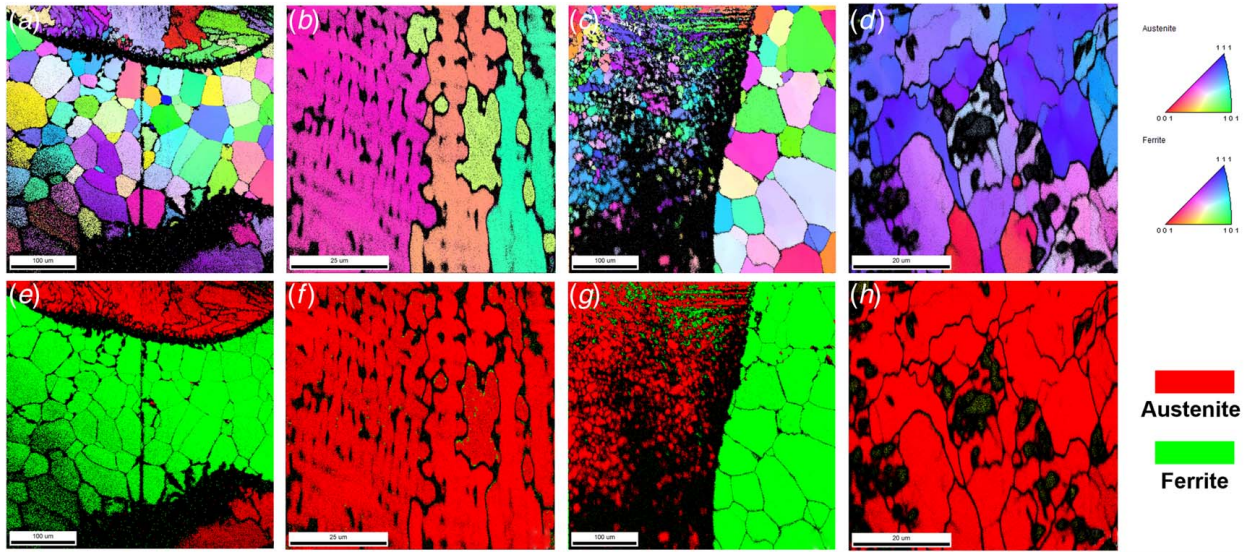


Fig. 9 EBSD measurement of carburized zone section: (a) and (b) show IPF of sample at 75 W from both sides, (c) and (d) present IPF of sample at 100 W from both sides, (b) and (d) are magnified characterization in carburized zone of (a) and (c) respectively, and (e)–(h) show the phase distribution of (a)–(d)

At a lower LED 15 kJ/m, with the distance increasing from this interface, the morphology of the carburized zone follows planar growth (A), cellular growth (B), columnar dendrite growth (C), and equiaxed dendrite growth (D) in Fig. 14(a). While at higher LED 20 kJ/m, this transformation stops mainly at cellular growth steps ((A) and (B)), and only a few dendrites can be found near the surface (Fig. 14(b)). This transformation has resulted from the element composition, temperature gradient (G), and solidification rate (R) [27]. For a given material, the ratio G/R is the governing parameter for the morphological solidification structure, cellular growth turns into dendrite growth when the ratio G/R is inferior to a critical value [31,32]. In the molten pool at 15 kJ/m, the undercooling is more pronounced and the ratio G/R decreases from the interface liquid/solid to the center, where cellular growth transforms into columnar dendrite growth. An increase in LED

leads to a lower cooling rate and a higher G/R [33], thus the carburized zone at 20 kJ/m presents a cell-dominated morphology, and only a few dendrites are found near the surface. Also, because the molten pool is deeper and thus poorer in carbon at higher LED, the constitutional undercooling becomes less important upon solidification, which favors the formation of cellular grains.

Austenitic grains are developed in the first place during the cooling cycle and excess carbon atoms are rejected to the grain boundaries. Numerous carbides are formed and inhibit the grain coarsening [34], which is the reason why there is a contrast in grain size between carburized zone and HAZ. While carbides are discretely distributed at grain boundaries and inside cellular grains at higher LED, a large quantity of eutectic structure is formed in the interdendritic network at lower LED. BSE and EDS results both show that Cr is richer in interdendritic regions and grain boundaries, it can be assumed that they form chromium-rich carbides like $M_{23}C_6$, which is the most common carbide in austenitic structures [23], but the exact type of carbides need to be investigated further. This segregation is observed in other studies where the ferrite promoting element Cr is richer in the interdendritic region

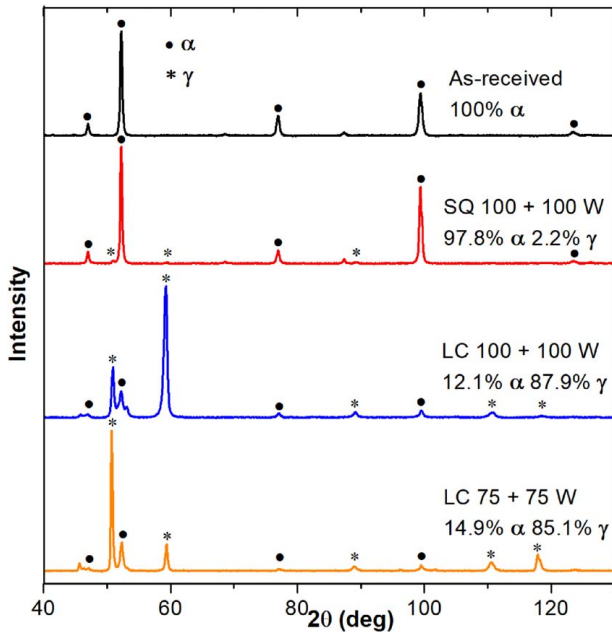


Fig. 10 XRD patterns and phase composition of samples treated under different conditions

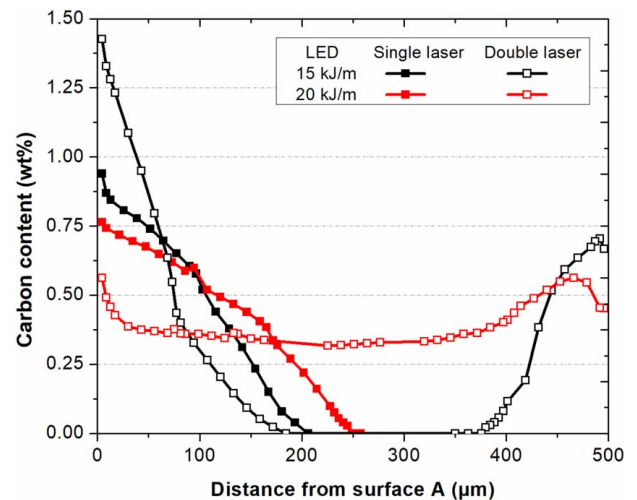


Fig. 11 Carbon mass fraction through the thickness of single and double laser treated samples measured by GD-OES

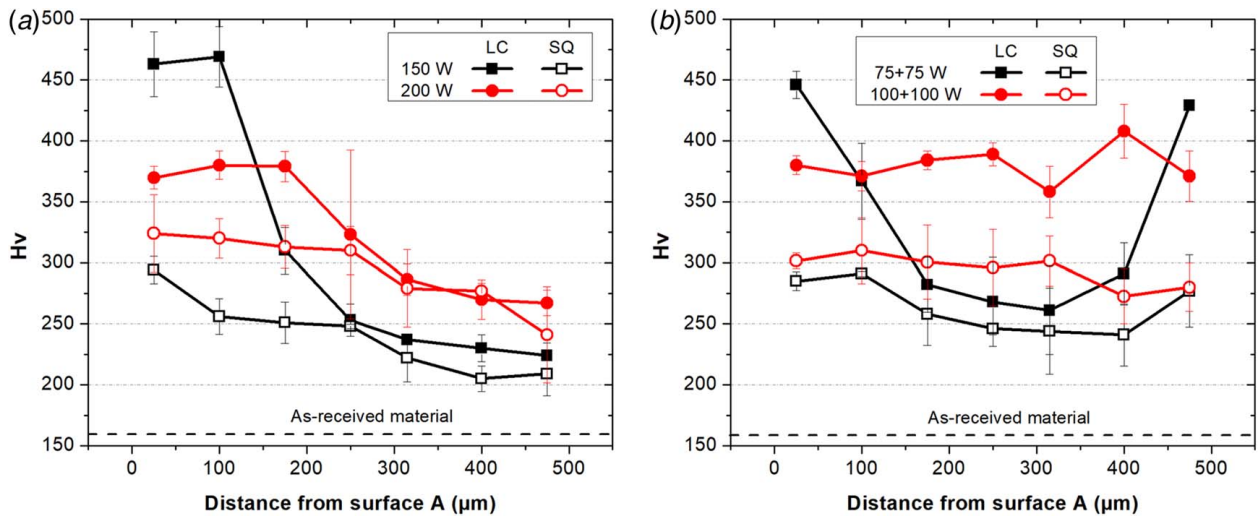


Fig. 12 Microhardness along laser beam center in the section (a) single laser treatment and (b) double laser treatment

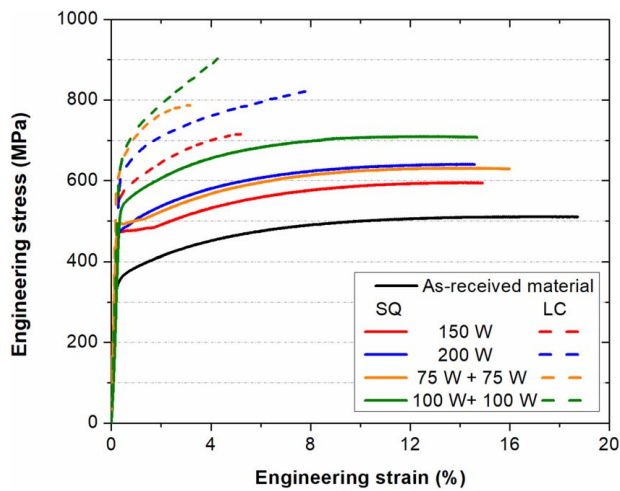


Fig. 13 Tensile test results of SQ and LC samples

contrary to the dendritic region [35]. It can also be assumed that the eutectic structure in Fig. 8 is composed of α -Fe and carbides from XRD analysis. This interdendritic eutectic solidification is observed in high-alloyed steels and its constitution varies according to the initial element composition in the melting pool [35]. In the present study, the interdendritic region exhibits a pearlite structure, and ledeburite can be observed in the case of more carbon dissolved into the bulk, such as carburizing process of cast iron [14].

Delta ferrite is found to be surrounded by austenite in EBSD images (Figs. 9(c) and 9(g)) at 20 kJ/m with the double laser

configuration. Delta ferrite appears widely in stainless steel welds and the content increases with the cooling rate due to the incomplete transformation $\delta \rightarrow \gamma$ [29]. By using the Schaeffler diagram [36] and taking the carbon content in the FZ at approximately 0.4% in Fig. 11, the equivalent of chromium (Cr_{eq}) and nickel (Ni_{eq}) can be calculated as Eqs. (3) and (4).

$$Cr_{eq} = \% Cr + \% Mo + 1.5 * \% Si + 0.5 * \% Nb = 19.15\% \quad (3)$$

$$Ni_{eq} = \% Ni + 30 * \% C + 0.5 * \% Mn = 12.39\% \quad (4)$$

The Cr_{eq}/Ni_{eq} in this zone is around 1.5, which indicates that less than 5% delta ferrite will present in the carburized zone. Even though delta ferrite can reduce the microcracking and fracture during solidification, it can cause brittleness with long exposure in 300–500 °C (the so-called 475 °C brittleness) [29]. A structure similar to that of duplex stainless steel appears in the FZ, which could be controlled more accurately by optimizing the experimental parameters. For other LC conditions, because the carbon content is even higher, the value of Cr_{eq}/Ni_{eq} is less than 1.3, thus the FZ is almost entirely austenitic [29].

The laser carburization process has an important hardening effect on chosen ferritic stainless steel according to the Y_s and UTS results in Table 3. The authors' earlier result [22] finds that the laser process without added graphite increases the microhardness at most by 90%. With graphite coating, the microhardness is improved to 450 Hv in dendritic microstructure and 380 Hv in cellular microstructure, which is 180% and 137% more than the as-received material. The most enhanced $\sigma_{0.2\%}$ and UTS are found when the bulk is entirely carburized and composed mostly of cellular grains with an increase of 90% and 85%, respectively. Both secondary phase strengthening and grain refining contribute to this

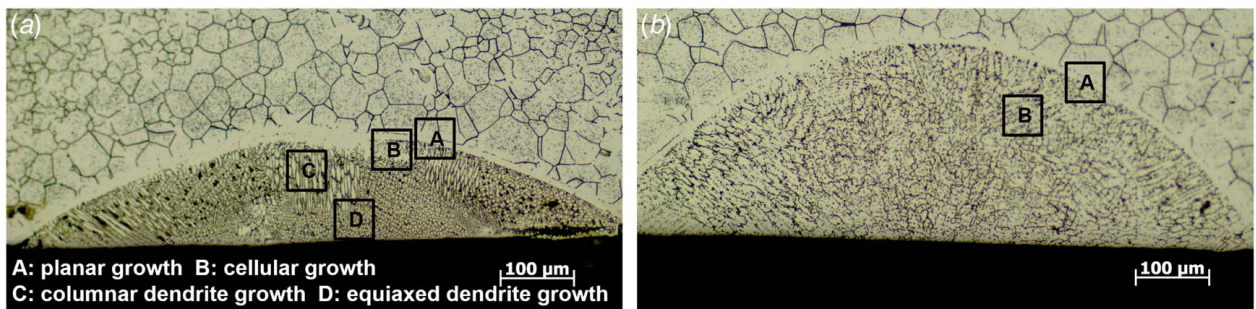


Fig. 14 Microstructure of carburized area by single laser treatment at (a) 15 kJ/m and (b) 20 kJ/m

improvement [34]. More strengthening carbides are formed in dendrite-dominated structure at lower LED and the higher cooling rate leads to more refined grains [31], which explain the difference in enhancement levels. At the same time, the ductility is seriously worsened due to strengthening phases. As the hard surface is positive to increase the fatigue life and wear resistance [14], laser carburization can be a potential choice for strengthening the surface of ferritic stainless steel and extending the service life of structural parts.

5 Conclusions

AISI 430 ferritic stainless steel sheets with graphite coating are carburized by direct laser irradiation in this study. Microstructural and mechanical properties are investigated to evaluate the strengthening effect of carburization. Some conclusions are drawn as follows:

- (1) Direct laser irradiation on graphite coating is efficient to carburize the substrate ferritic stainless steel within several hundred micron depths. The least carbon content in the carburized region is around 0.4% compared to 0.026% in the as-received material; the shallower the carburized region, the higher the carbon content.
- (2) The morphology of carburized zone depends on the ratio of temperature gradient and solidification rate caused by different LEDs. At lower LED, it exhibits mostly austenitic dendrites and eutectic interdendritic structures. At higher LED, cellular austenitic grains are formed with discrete carbides inside and at grain boundaries. Double laser treatment with suitable LED can lead to a uniformly carburized zone through the whole thickness.
- (3) As-received material is remarkably strengthened by the laser carburization process. Microhardness is improved to 469 Hv and 380 Hv respectively for dendritic microstructure and cellular microstructure compared to 160 Hv of as-received material. The $\sigma_{0.2\%}$ and UTS are increased by 90% and 85% at most. This improvement could be applied to strengthen the ferritic stainless steel parts' surface in order to increase fatigue and wear resistance.
- (4) At higher LED, a small quantity of delta ferrite is found among austenitic grains due to the rapid cooling and suitable C_{Teq}/Ni_{eq} value, which creates a duplex region. The formation of delta ferrite could be better controlled by adjusting the experimental parameters to achieve a desirable percentage.

Acknowledgment

This study was funded by Agence Nationale de la Recherche through the ANR JCJC SCOLASTIC (Systematic Computational Optimization and Local Laser Processing for Steel Based Architected Materials) project (Grant No. 16-CE08-0009).

Conflict of Interest

There are no conflicts of interest.

Data Availability Statement

The datasets generated and supporting the findings of this article are obtainable from the corresponding author upon reasonable request.

References

- [1] Cashell, K. A., and Baddoo, N. R., 2014, "Ferritic Stainless Steels in Structural Applications," *Thin-Walled Struct.*, **83**, pp. 169–181.
- [2] Sundqvist, J., Manninen, T., Heikkinen, H.-P., Anttila, S., and Kaplan, A. F. H., 2018, "Laser Surface Hardening of 11% Cr Ferritic Stainless Steel and Its Sensitisation Behaviour," *Surf. Coat. Technol.*, **344**, pp. 673–679.
- [3] Tadeipalli, L. D., Gosala, A. M., Kondamuru, L., Bairi, S. C., Subbiah, R., and Singh, S. K., 2020, "A Review on Effects of Nitriding of AISI409 Ferritic Stainless Steel," *Mater. Today Proc.*, **26**, pp. 1014–1020.
- [4] Hirata, T., Yamaguchi, T., Yokoyama, Y., and Hoshino, H., 2020, "Surface Modification by High-Speed Laser Gas Carburization in Low-Alloy Steel," *Mater. Lett.*, **280**, p. 128586.
- [5] Schaaf, P., Kahle, M., and Carpena, E., 2005, "Reactive Laser Synthesis of Carbides and Nitrides," *Appl. Surf. Sci.*, **247**(1–4), pp. 607–615.
- [6] Capello, E., and Previtali, B., 2009, "Enhancing Dual Phase Steel Formability by Diode Laser Heat Treatment," *J. Laser Appl.*, **21**(1), pp. 1–9.
- [7] Lapouge, P., Dirrenberger, J., Coste, F., and Schneider, M., 2019, "Laser Heat Treatment of Martensitic Steel and Dual-Phase Steel With High Martensite Content," *Mater. Sci. Eng. A*, **752**, pp. 128–135.
- [8] Kennedy, E., Byrne, G., and Collins, D. N., 2004, "A Review of the Use of High Power Diode Lasers in Surface Hardening," *J. Mater. Process. Technol.*, **155–156**, pp. 1855–1860.
- [9] Maharjan, N., Zhou, W., and Wu, N., 2020, "Direct Laser Hardening of AISI 1020 Steel Under Controlled Gas Atmosphere," *Surf. Coat. Technol.*, **385**, p. 125399.
- [10] Höche, D., Kaspar, J., and Schaaf, P., 2015, "Laser Nitriding and Carburization of Materials," *Laser Surface Engineering*, J. Lawrence and D. G. Waugh, eds., Elsevier, New York, pp. 33–58.
- [11] Saleh, A. F., Abboud, J. H., and Benyounis, K. Y., 2010, "Surface Carburizing of Ti-6Al-4V Alloy by Laser Melting," *Opt. Lasers Eng.*, **48**(3), pp. 257–267.
- [12] Seo, D. M., Hwang, T. W., and Moon, Y. H., 2019, "Carbonitriding of Ti-6Al-4V Alloy Via Laser Irradiation of Pure Graphite Powder in Nitrogen Environment," *Surf. Coat. Technol.*, **363**, pp. 244–254.
- [13] Makuch, N., Kulka, M., Dziarski, P., and Przystacki, D., 2014, "Laser Surface Alloying of Commercially Pure Titanium With Boron and Carbon," *Opt. Lasers Eng.*, **57**, pp. 64–81.
- [14] Chen, Z., Zhou, T., Zhao, R.-Y., Zhang, H.-F., Lu, S.-C., Yang, W.-S., and Zhou, H., 2015, "Improved Fatigue Wear Resistance of Gray Cast Iron by Localized Laser Carburizing," *Mater. Sci. Eng. A*, **644**, pp. 1–9.
- [15] Sui, Q., Zhou, H., Bao, H., Zhang, P., Yuan, Y., and Meng, C., 2018, "Wear Behavior of Quenched Iron With Various Shapes and Unit Processed Through Two-Step Laser Alloying of C Powder," *Opt. Laser Technol.*, **104**, pp. 103–111.
- [16] Tayal, M., and Mukherjee, K., 1994, "Selective Area Carburizing of Low Carbon Steel Using an Nd: YAG Laser," *Mater. Sci. Eng. A*, **174**(2), pp. 231–236.
- [17] Katsamas, A. I., and Haidemenopoulos, G. N., 2001, "Laser-Beam Carburizing of Low-Alloy Steels," *Surf. Coat. Technol.*, **139**(2–3), pp. 183–191.
- [18] Yao, J., Zhang, Q., Gao, M., and Zhang, W., 2008, "Microstructure and Wear Property of Carbon Nanotube Carburizing Carbon Steel by Laser Surface Remelting," *Appl. Surf. Sci.*, **254**(21), pp. 7092–7097.
- [19] Liu, Z., Zhang, S., Wang, S., Peng, Y., Gong, J., and Somers, M. A. J., 2020, "On the Fatigue Behavior of Low-Temperature Gaseous Carburized 316L Austenitic Stainless Steel: Experimental Analysis and Predictive Approach," *Mater. Sci. Eng. A*, **793**, p. 139651.
- [20] Rovani, A. C., Breganon, R., de Souza, G. S., Brunatto, S. F., and Pintaúde, G., 2017, "Scratch Resistance of Low-Temperature Plasma Nitrided and Carburized Martensitic Stainless Steel," *Wear*, **376–377**, pp. 70–76.
- [21] Scheuer, C. J., Cardoso, R. P., Pereira, R., Mafrá, M., and Brunatto, S. F., 2012, "Low Temperature Plasma Carburizing of Martensitic Stainless Steel," *Mater. Sci. Eng. A*, **539**, pp. 369–372.
- [22] Wang, Z., Dirrenberger, J., Lapouge, P., and Dubent, S., 2022, "Laser Treatment of 430 Ferritic Stainless Steel for Enhanced Mechanical Properties," *Mater. Sci. Eng. A*, **831**, p. 142205.
- [23] Vander Voort, G. F., Lucas, G. M., and Manilova, E. P., 2004, "Metallography and Microstructures of Stainless Steels and Maraging Steels," *Metallography and Microstructures*, GF Vander Voort, ed., ASM International, Materials Park, OH, pp. 670–700.
- [24] Narazaki, M., Kogawara, M., Ming, Q., and Watanabe, Y., 2009, "Measurement and Database Construction of Heat Transfer Coefficients of Gas Quenching," *Stroj. Vestn.*, **55**(3), pp. 167–173.
- [25] American Welding Society, 2018, "Alloy Composition and Critical Temperatures in Type 410 Steel Welds," *Weld. J.*, **97**(10), pp. 286–296.
- [26] Capdevila, C., Caballero, F. G., and de Andrés, C. G., 2002, "Determination of Ms Temperature in Steels: A Bayesian Neural Network Model," *ISIJ Int.*, **42**(8), pp. 894–902.
- [27] Khalfallah, I. Y., Rahoma, M. N., Abboud, J. H., and Benyounis, K. Y., 2011, "Microstructure and Corrosion Behavior of Austenitic Stainless Steel Treated With Laser," *Opt. Laser Technol.*, **43**(4), pp. 806–813.
- [28] Hao, Y., Li, J., Li, X., Liu, W., Cao, G., Li, C., and Liu, Z., 2020, "Influences of Cooling Rates on Solidification and Segregation Characteristics of Fe-Cr-Ni-Mo-N Super Austenitic Stainless Steel," *J. Mater. Process. Technol.*, **275**, p. 116326.
- [29] Wegrzyn, T., 1992, "Delta Ferrite in Stainless Steel Weld Metals," *Weld. Int.*, **6**(9), pp. 690–694.
- [30] Nair, A. M., Muvvala, G., and Nath, A. K., 2019, "A Study on In-Situ Synthesis of TiCN Metal Matrix Composite Coating on Ti-6Al-4V by Laser Surface Alloying Process," *J. Alloys Compd.*, **810**, p. 151901.
- [31] Blecher, J. J., Palmer, T. A., and DeRoy, T., 2014, "Solidification Map of a Nickel-Base Alloy," *Metall. Mater. Trans. A*, **45**(4), pp. 2142–2151.
- [32] Berjeza, N. A., Velikevitch, S. P., Mazhukin, V. I., Smurov, I., and Flamant, G., 1995, "Influence of Temperature Gradient to Solidification Velocity Ratio on the

- Structure Transformation in Pulsed- and CW-Laser Surface Treatment,” *Appl. Surf. Sci.*, **86**(1–4), pp. 303–309.
- [33] Li, Z., Yu, G., He, X., Li, S., Li, H., and Li, Q., 2019, “Study of Thermal Behavior and Solidification Characteristics During Laser Welding of Dissimilar Metals,” *Results Phys.*, **12**, pp. 1062–1072.
- [34] Jiang, P. F., Zhang, C. H., Zhang, S., Zhang, J. B., Chen, J., and Liu, Y., 2020, “Microstructure Evolution, Wear Behavior, and Corrosion Performance of Alloy Steel Gradient Material Fabricated by Direct Laser Deposition,” *J. Mater. Res. Technol.*, **9**(5), pp. 11702–11716.
- [35] Zhang, H., Zhang, C. H., Wang, Q., Wu, C. L., Zhang, S., Chen, J., and Abdullah, A. O., 2018, “Effect of Ni Content on Stainless Steel Fabricated by Laser Melting Deposition,” *Opt. Laser Technol.*, **101**, pp. 363–371.
- [36] Schaeffler, A. L., 1949, “Constitution Diagram for Stainless Steel Weld Metal,” *Met. Prog.*, **56**(11), p. 680.